A multi-level cell for ultra-scaled STT-MRAM realized by back-hopping

M. Bendra [a,b,*], R.L. de Orio [a,b], S. Selberherr [b], W. Goes [c], V. Sverdlov [a,b]

[a] *Christian Doppler Laboratory for Nonvolatile Magnetoresistive Memory and Logic, Gußhausstraße 27-29, Wien, A-1040, Austria*
[b] *Institute for Microelectronics, TU Wien, Gußhausstraße 27-29, Wien, A-1040, Austria*
[c] *Silvaco Europe Ltd., Compass Point, St Ives, Cambridge, PE27 5JL, United Kingdom*

ARTICLE INFO

ABSTRACT

The development of advanced magnetic tunnel junctions with a footprint in the single-digit nanometer range can be achieved using structures with an elongated and composite ferromagnetic free layer. Using advanced modeling techniques, we investigated the back-hopping effect in ultra-scaled STT-MRAM devices, defined as the unintended switching of the last part of the free layer, leading to an undesired magnetization state of the free layer. To understand the switching of the free layer, the torque acting on both parts of the composite-free layer must be studied in detail. A reduction in the size of MRAM components to increase the memory density may lead to back-hopping. However, the observed back-hopping effect can also be exploited for the realization of multi-level cells. For this purpose, we have carefully investigated the switching behavior of a device with several tunnel barrier interfaces and a few nanometers in diameter. Our studies on ultra-scaled STT-MRAM devices highlight the significant back-hopping effect which, when harnessed, can enable multi-bit cells with four distinct states, enhancing storage and functionality. These insights are pivotal for the design and optimization of future miniaturized spintronics devices.

1. Introduction

Spin-transfer torque magnetoresistive random access memory (STT-MRAM) is one of the most promising candidates for nonvolatile memory technologies. In particular, STT-MRAM technology is attractive for Computing-in-Memory concepts [1], embedded automotive systems [2], low-latency industrial applications [3], last-level cache for microprocessors [4], and high-density MRAM arrays [5]. These diverse applications highlight the potential of STT-MRAM technology in different fields and its versatility in meeting various requirements.

An STT-MRAM cell consists of several layers, including a CoFeB reference layer (RL) and a free magnetic layer (FL) separated by an MgO tunnel barrier (TB), which form a magnetic tunnel junction (MTJ). To increase the perpendicular magnetic anisotropy, the FL, typically composed of two CoFeB layers and a thin metal buffer, is interfaced with a second MgO layer [6]. Elongating the FL and introducing additional MgO layers allows to even further increase the perpendicular anisotropy, while also reducing the cell diameter [7].

Back-hopping refers to the unwanted switching of the magnetization state in the fixed layer of a standard MTJ. In our study, we harness this effect in a composite FL. When the length of the FL falls below a certain threshold or at higher current densities [8], we utilize back-hopping to switch the magnetization state of the FL section. This effect is driven by reduced anisotropy in the FL due to its shorter length and increased

spin-transfer torques at higher current densities. Consequently, the FL magnetization reverts to its original state. By properly adjusting the polarization of the TB, this back-hopping effect can be exploited to realize multi-level cells (MLC), thereby turning a potential drawback into a significant advantage for multi-bit memory applications.

To further enhance memory density, a MLC based on more than one MTJ is proposed [9]. However, the implementation of a MLC requires careful tuning of the characteristics of each MTJ, leading to the formation of multiple stable states [10]. Therefore, there is a need to understand the magnetization dynamics of magnetic materials related to the performance of MTJs in order to accurately design a MLC. The structure of the paper is as follows: Section 2 discusses the micromagnetics model used for simulating the magnetization dynamics. Section 3 presents the analysis of the back-hopping effect in ultra-scaled STT-MRAM devices. Section 4 explores the application of the back-hopping effect to achieve multi-level cells. Finally, Section 4 concludes the findings and outlines potential future work.

2. Micromagnetics model

For an accurate representation of MLCs, it is imperative to precisely evaluate the spin-transfer torques, which are fundamental to

---

* Corresponding author at: Institute for Microelectronics, TU Wien, Gußhausstraße 27-29, Wien, A-1040, Austria.
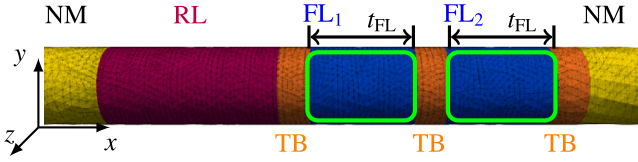*E-mail address:* bendra@iue.tuwien.ac.at (M. Bendra).

Fig. 1. A simplified mesh representation of an ultra-scaled MRAM cell. This composite structure consists of a CoFeB (5)|MgO (0.9)|CoFeB (3)|MgO (0.9)|CoFeB (3)|MgO (0.9) MTJ connected to normal metal contacts (50), where the numbers in parentheses indicate the length of each layer in nanometers. The diameter is 2.3 nm. A bias of 1.5 V is applied across the structure. The color coding is as follows: purple for the RL, blue for the FL, orange for the TB, and yellow for the non-magnetic contacts (NM). The green framed section denotes the FL segments for FL$_1$ and FL$_2$, with the length t_{FL}.

the memory's functionality. Our micromagnetics model incorporates novel approaches to capture the intricacies of magnetization dynamics in MTJs with composite FLs. While some components, such as the Landau–Lifshitz–Gilbert (LLG) equation, are widely used in the spintronics community, our specific formulation of the spin-transfer torque via the non-equilibrium spin accumulation and its integration into a finite element method (FEM) solver represents a novel contribution. Unlike previous models, our methodology integrates a coupled spin and charge drift–diffusion framework with boundary conditions tailored for multilayered MTJs. This allows us to exploit the back-hopping effect to achieve MLC by providing a more precise depiction of spin-transfer torques and their impact on MLC behavior. We introduce a comprehensive modeling methodology that captures the vital physical phenomena as described in Eqs. (1)–(7). Within this framework, the LLG Eq. (1) is numerically solved to depict the normalized magnetization dynamics. The resolution of the LLG equation is facilitated through the FEM. This computational procedure is executed in C++ leveraging the open-source FEM library, MFEM [11]. The implementation can be accessed as reported in [12].

$$\frac{\partial \mathbf{m}}{\partial t} = -\gamma \mu_0 \mathbf{m} \times \mathbf{H}_{\text{eff}} + \alpha \mathbf{m} \times \frac{\partial \mathbf{m}}{\partial t} + \frac{1}{M_S} \mathbf{T_S} \tag{1}$$

The effective magnetic field, denoted as $\mathbf{H}_{\text{eff}}$, is a summation of the magnetic anisotropy field, the exchange field, and the demagnetization field. For the computation of the demagnetization field over discontinuous magnetic domains, a combined methodology incorporating both, the boundary element method (BEM) and the FEM, is utilized [13]. Such a methodology offers applicability to intricate discontinuous magnetic topologies, such as synthetic antiferromagnets. The respective computational implementation can be accessed as reported in [14]. Parameters are defined as follows: γ stands for the gyromagnetic ratio, μ_0 signifies the vacuum permeability, α represents the Gilbert damping constant, $\mathbf{M}$ denotes the magnetization vector, which is a function of both time and spatial position, $\mathbf{m}$ is the normalized magnetization vector given by $\mathbf{m} = \mathbf{M}/M_S$, and M_S corresponds to the saturation magnetization value. The first term on the right-hand side of the LLG equation describes the precessional dynamics, wherein the magnetization vector undergoes a precessional motion around the $\mathbf{H}_{\text{eff}}$. The subsequent term characterizes a damping mechanism which endeavors to orient the magnetization in congruence with the $\mathbf{H}_{\text{eff}}$. The last term models the spin-transfer torque contributions.

In the simulation of switching dynamics in ultra-scaled MRAM cells, we formulate the spin-transfer torque, denoted as $\mathbf{T_S}$, derived from the relation:

$$\mathbf{T_S} = -\frac{D_e}{\lambda_J^2} \mathbf{m} \times \mathbf{S} - \frac{D_e}{\lambda_\varphi^2} \mathbf{m} \times (\mathbf{m} \times \mathbf{S}) \tag{2}$$

Here, λ_J represents the exchange length, λ_φ denotes the spin dephasing length, D_e is the electron diffusion constant, and $\mathbf{S}$ symbolizes the spin accumulation. Notably, $\mathbf{S}$ originates when an electric current traverses the MRAM structure and undergoes polarization by its magnetic layers.

For the determination of $\mathbf{S}$, it is imperative to employ the spin and charge drift–diffusion framework, as detailed in Eqs. (3) through (5). This approach is an accurate representation of the charge and spin transport mechanisms within a nanoscale magnetic tunnel junction.

$$D_e \left(\frac{\mathbf{S}}{\lambda_{sf}^2} + \frac{\mathbf{S} \times \mathbf{m}}{\lambda_J^2} + \frac{\mathbf{m} \times (\mathbf{S} \times \mathbf{m})}{\lambda_\varphi^2} \right) = -\nabla \cdot \mathbf{J_S} \tag{3}$$

$$\mathbf{J_S} = -\frac{\mu_B}{e} \beta_\sigma \left(\mathbf{J_C} \otimes \mathbf{m} + \beta_D D_e \frac{e}{\mu_B} [(\nabla \mathbf{S}) \mathbf{m}] \otimes \mathbf{m} \right) - D_e \nabla \mathbf{S} \tag{4}$$

$$\mathbf{J_C} = \sigma E - \beta_D D_e \frac{e}{\mu_B} [(\nabla \mathbf{S}) \mathbf{m}] \tag{5}$$

$\mathbf{J_C}$ defines the flow of electric charge, λ_{sf} denotes the length associated with the process of spin-flip, σ represents the electrical conductivity, E stands for the electric field, β_D and β_σ are coefficients related to the polarization, e corresponds to the elementary charge, μ_B is the Bohr magneton, and $\mathbf{J_S}$ is the tensor describing the flow of spin.

A pivotal electrical characteristic of a MTJ is the Tunneling Magnetoresistance (TMR) phenomenon. This phenomenon quantifies a significant variation in electrical resistance between the anti-parallel (AP) and parallel (P) orientations of a MTJ. The TMR ratio is mathematically defined as:

$$\text{TMR} = \frac{R_{AP} - R_P}{R_P} \tag{6}$$

We have extended the method to MTJs by conceptualizing the TB as an imperfect conductor with a resistivity described by Eq. (7), meaning that its local resistance depend on the relative alignment of the FL magnetization [15].

$$\sigma(\theta) = \frac{\sigma_P + \sigma_{AP}}{2} \left(1 + \left(\frac{\text{TMR}}{2 + \text{TMR}} \right) \cos \theta \right) \tag{7}$$

Our model accurately describes the accumulation of spin and the corresponding torques exerted on the magnetization. The TMR aptly elucidates the modulation of conductivity and the density of charge current. Furthermore, we put forth a formulation for the density of spin current at the TB interfaces by means of interface polarization parameters and out-of-plane spin polarization coefficients. This methodology was applied to a MTJ structure comprising a free layer composed of two elongated ferromagnetic components.

We supplement the model with appropriate boundary conditions for the density of spin current $\mathbf{J_S^{TB}}$ at the TB interfaces to account for the torque's dependence on the specific relative magnetization orientation inherent to MTJs [15]:

$$\mathbf{J_C^{TB}} = J_0(V)(1 + P_{RL} P_{FL} \cdot \cos \theta) \tag{8}$$

$$\mathbf{J_S^{TB}} = -\frac{\mu_B}{e} \frac{\mathbf{J_C^{TB}} \cdot \mathbf{n}}{1 + P_{RL} P_{FL} \mathbf{m_{RL}} \cdot \mathbf{m_{FL}}} \cdot [P_{RL} \mathbf{m_{RL}} + \tag{9}$$

$$+ P_{FL} \mathbf{m_{FL}} + 1/2 (P_{RL}^\eta P_{RL} - P_{FL}^\eta P_{FL}) \mathbf{m_{RL}} \times \mathbf{m_{FL}}]$$

Eq. (8) depicts the association between the density of charge current at the interface, denoted as $\mathbf{J_C^{TB}}$, with the RL and FL polarization parameters and the angle between their respective magnetization vectors. It expresses the charge current density at the interface as being directly proportional to a voltage-dependent component of the current density $J_0(V)$. This product is further influenced by the cosine of the angle between the magnetizations of RL and FL and their corresponding in-plane Slonczewski polarization parameters P_{RL} and P_{FL}. The boundary condition, represented as Eq. (9), is crucial for accurately assessing the spin current and the spin accumulation in the RL and the FL, respectively. Here, $\mathbf{n}$ signifies the interface normal, $\mathbf{m_{RL(FL)}}$ stands for the magnetization of the RL and the FL, $P_{RL(FL)}$ denote the in-plane Slonczewski polarization parameters, P_{RL}^η and P_{FL}^η are parameters associated with out-of-plane polarization, and e denotes the elementary charge.

Through the utilization of Eq. (9), we expound upon the transport of spin and charge intertwined with the magnetization in diverse

Table 1
Simulation parameters.

Parameter	Value
Gilbert damping, α	0.015
Gyromagnetic ratio, γ	$1.76 \cdot 10^{11}$ rad s^{-1} T^{-1}
Saturation magnetization, M_S	$0.81 \cdot 10^6$ A m^{-1}
Exchange constant, A	$2 \cdot 10^{-11}$ J m^{-1}
Free layer length, t_{FL}	$2-5$ nm
Interface anisotropy, K_i	$1.53 \cdot 10^{-3}$ J m^{-2}
Uniaxial anisotropy constant, K	K_i/t_{FL}
Current spin polarization, β_σ	0.7
Diffusion spin polarization, β_D	1.0
Electron diffusion coefficient, D_e	$1 \cdot 10^{-2}$ m^2 s^{-1}
Spin-flip length, λ_{sf}	10 nm
Exchange length, λ_J	0.8 nm
Spin dephasing length, λ_φ	0.4 nm
Electrical resistance in the anti-parallel state, R_{AP}	750 kΩ
Electrical resistance in the parallel state, R_P	410 kΩ

stacks of MTJs and metallic spin valves employing a coherent drift–diffusion methodology. This methodology offers a meticulous analysis of the sequential switching of a composite FL comprising two elongated ferromagnetic sections, FL$_1$ and FL$_2$, separated by a tunnel junction. An accessible computational implementation [16] is available for computing spin-transfer torques in magnetic multilayer configurations. All in all, our approach offers the potential for an accurate and all-encompassing comprehension of spin and charge transport in MTJs, thereby contributing to the advancement of cutting-edge MRAM technology.

3. Results

The results of the switching simulations performed with the structure shown in Fig. 1 are detailed below. We assessed the behavior employing alternative material parameters compared to those used in [17]. These parameters are presented in Table 1 and are sourced from the Boris Computational Spintronics material database [18].

In Fig. 2 the magnetization trajectories for the switching from anti-parallel (AP) to parallel (P) and from P to AP with symmetric FL configurations are displayed. The applied bias is 1.5 V or −1.5 V depending on the magnetization switching direction, P to AP or AP to P.

Fig. 2(a) reports, that successful switching of the FL from AP to P is always obtained. The deviation in the final state for $t_{FL} = 2$ nm and $t_{FL} = 3$ nm signifies a state resembling a canted position. As the bias continues to be applied, the magnetization remains in this end state. Discontinuing the bias would cause the structure to settle into the final state with $m_x = 1$. Fig. 2(b) reveals that none of the structures successfully transitions from P to AP. For a length of $t_{FL} = 2$ nm, both FL parts initiate their transition simultaneously. However, FL$_1$ completes the transitions before FL$_2$, causing FL$_1$ to push FL$_2$ back to its initial position, resulting in an average magnetization around $m_x = 0$. For the other structures, a sequential switching pattern is observed. FL$_2$ transitions first, then FL$_1$. But before FL$_1$ can fully reach its end state of AP to RL, the torques changes depending on the FL$_1$ orientation and reverts FL$_2$ back to its original state.

The differences in the response times of the cells are due to the different uniaxial anisotropies which depend on the length of the layer. A shorter layer possesses a reduced energy barrier separating the two magnetization configurations, so that the speed of the response is improved in the case of the shorter layer.

In Fig. 3 we report switching realizations, where we modeled the polarization of the TBs, such that the TB in the middle of the FL is the higher one. In Fig. 3(a), every structure successfully switches, except when the FL length is 2 nm or 3 nm. At a FL length of 2 nm, the magnetization displays characteristics of a vortex state while the bias remains active. Turning off the bias would not result in reaching
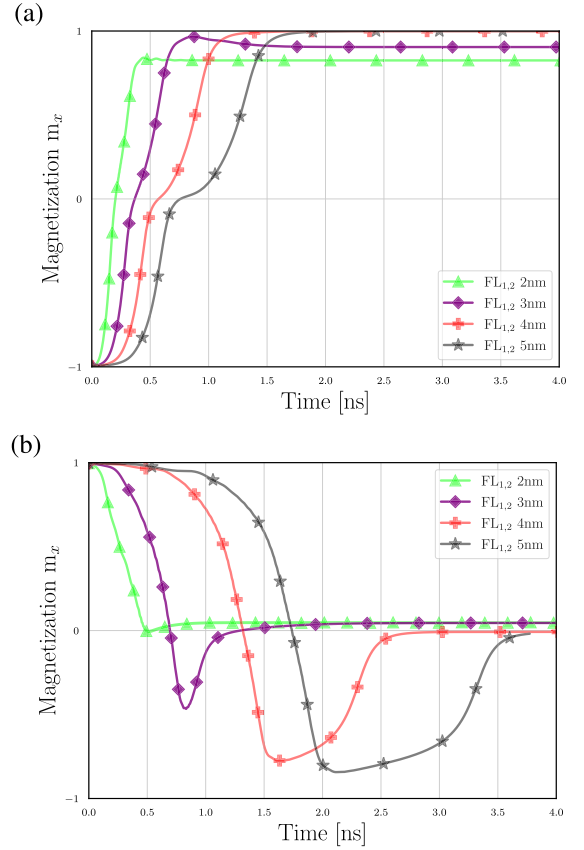

(a)

(b)

Fig. 2. Magnetization trajectories for the switching from (a) AP to P and (b) P to AP for different combinations of FL lengths. The polarization of the TB is 0.62, 0.57, and 0.2, in order from left to right in Fig. 1.

the intended state. When the FL length is 3 nm, the magnetization undergoes a cyclical switching pattern. The sequence involves FL$_2$ switching first, followed by FL$_1$, after which FL$_1$ reverts to its original position and then FL$_2$ follows.

In Fig. 4, the spin-torque is calculated based on the spin-current boundary condition provided by Eq. (9). The red arrows indicate a position near the end of the AP to P transition, consistent with Fig. 2(a) and 3(a). The FL magnetization has a subtle five-degree tilt in the z-direction. The solid line is in relation to the polarization presented in Fig. 2, while the dotted line is associated with the polarization in Fig. 3. The field-like and damping-like components in FL$_2$ try to align its magnetization in the positive x-direction, while the damping-like and field-like components in FL$_1$ try to initiate the back-hopping of it.

An elevated polarization in the central TB indicates an increase in spin-polarized electrons, which results in a more pronounced spin current across the barrier. This amplifies the transfer of angular momentum to the magnetic moment of the FLs. The following slight increase in torque is sufficient to challenge the weak anisotropy observed in Fig. 3(a), initiating a back-and-forth switching.

In the AP configuration, the pre-established direction for the voltage flow is negative, which corresponds to the traditional 'positive' direction in terms of electron flow. Thus, the electrons move in the opposite direction to the defined voltage flow. In this AP setup the RL exerts a torque on FL$_1$, driving it in the positive x-direction to align it parallel with the RL. At the same time FL$_2$ exerts a torque on FL$_1$ in the same direction, establishing an anti-parallel orientation with respect to FL$_2$. The cumulative effect of these torques prompts the initial switch of FL$_1$. As this happens, the torque applied from FL$_1$ towards FL$_2$ promotes parallel alignment of the two magnetization vectors, maintaining FL$_2$ in its original state. However, upon the switch of FL$_1$'s magnetization,
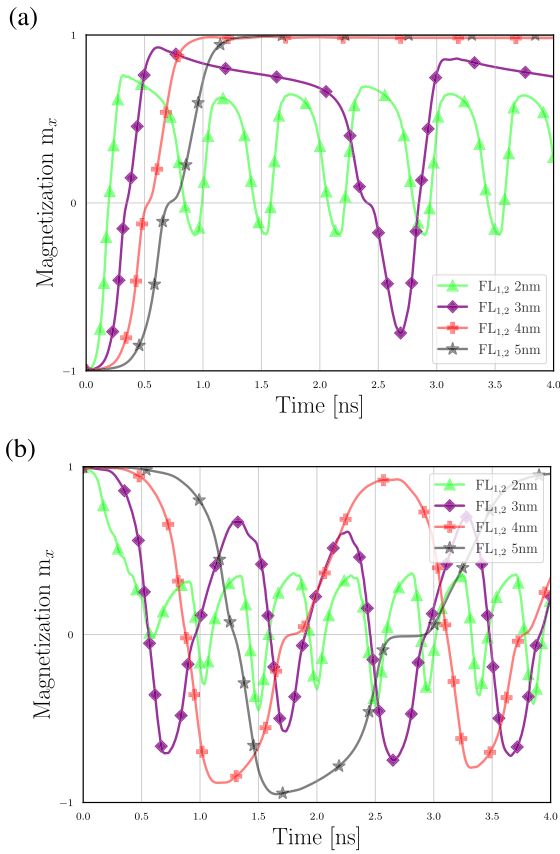
(a)

(b)

Fig. 3. Magnetization trajectories for the switching from (a) AP to P and (b) P to AP for different combinations of FL lengths, where we applied the same methodology as in Fig. 1, but with increasing polarization of TB in the middle of the FL. The polarization of the TB is 0.5, 0.9, and 0.2, in order from left to right in Fig. 1. In addition, the symmetric structure with 3 nm long FLs has the best prerequisites for a MLC.
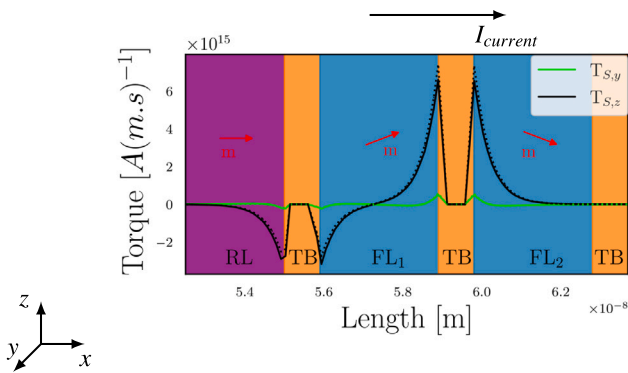

Fig. 4. The torque computed with the spin-current boundary condition (9) for an MTJ with semi-infinite ferromagnetic layers. Red arrows signify the direction of magnetization in the ferromagnetic segments. The plot shows along the central axis of the structure, $T_{S,y}$ represents a field-like component, while $T_{S,z}$ corresponds to a damping-like component of the spin torque. The arrow $I_{current}$, denotes the electron direction. Solid lines in this figure indicate TB polarizations of 0.62, 0.57, and 0.2 from left to right in Fig. 1, while the dotted line showcases TB polarizations of 0.5, 0.9, and 0.2 in the corresponding order.

the torque imposed on FL$_2$ undergoes a sign change, compelling it to switch subsequently too.

Fig. 3(b) illustrates the back-hopping effect. The structures with 4 nm and 5 nm length show continuous transitions between the sequence of states as long as the bias is applied. The sequential switching procedure of the composite FL is as following, during the switching from
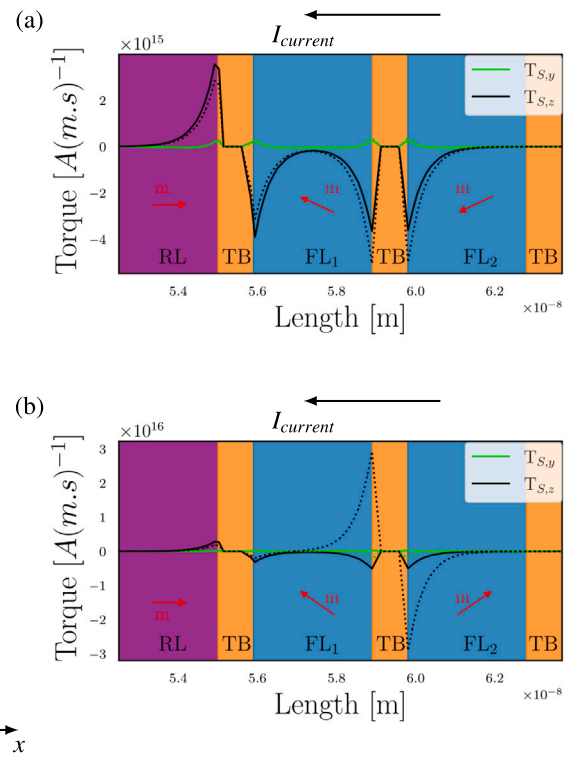
(a)

(b)

Fig. 5. Calculation of the spin-torque is performed using the spin-current boundary condition equation, as given in Eq. (9). Red arrows signify the direction of magnetization in the ferromagnetic segment. (a) A near-final position in the P to AP transition. (b) FL$_2$ nearly fully reversed due to back-hopping. The plot shows along the central axis of the structure, $T_{S,y}$ represents a field-like component, while $T_{S,z}$ corresponds to a damping-like component of the spin torque. The arrow $I_{current}$, denotes the electron direction. Solid lines in this figure indicate TB polarizations of 0.62, 0.57, and 0.2 from left to right in Fig. 1, while the dotted line showcases TB polarizations of 0.5, 0.9, and 0.2 in the corresponding order.

the P to AP configuration, the process evolves in an opposite manner. The torque from FL$_2$ acting on FL$_1$ opposes that from the RL. On the other hand, the torque from FL$_1$ acting on FL$_2$ supports magnetization inversion, prompting FL$_2$ to switch initially. After FL$_2$'s switch, the torques from both FL$_2$ and the RL act on FL$_1$ in the same direction, finalizing the switching process. The structures with 4 nm and 5 nm exhibit a seamless transition across the four magnetic states, making them optimal candidates for MLC applications. A notable distinction between these two structures lies in the oscillation frequency during their state transitions.

In Fig. 5, we draw a comparison similar to Fig. 4. Utilizing the spin-current boundary condition from Eq. (9), the spin-torque is determined. The red arrows mark an almost-final position during the P to AP transition, in line with Fig. 2(b) and 3(b). As previously the magnetization has a slightly tilted angle of five degrees in the z-direction. The continuous line references the polarization presented in Fig. 2, while the dotted line is in relation to Fig. 3.

As the applied bias is maintained, the elevated polarization in the middle TB causes the FL$_2$ magnetization to reverse, leading to its back-hopping. Fig. 5(a) displays damping-like and field-like components on FL$_1$ striving for an AP setup with the RL. Contrarily, the damping-like and field-like components from FL$_2$ favor the parallel configuration, pushing FL$_2$ back to its initial stance, thus inducing back-hopping. The marginal torque amplification overcomes the FL's weak anisotropy, prompting FL$_2$'s back-hopping. However, Fig. 5(b) shows the almost complete reversal of FL$_2$, we distinguish the stability of the position in Fig. 2(b) at around $m_x = 0$. The damping-like and field-like components,
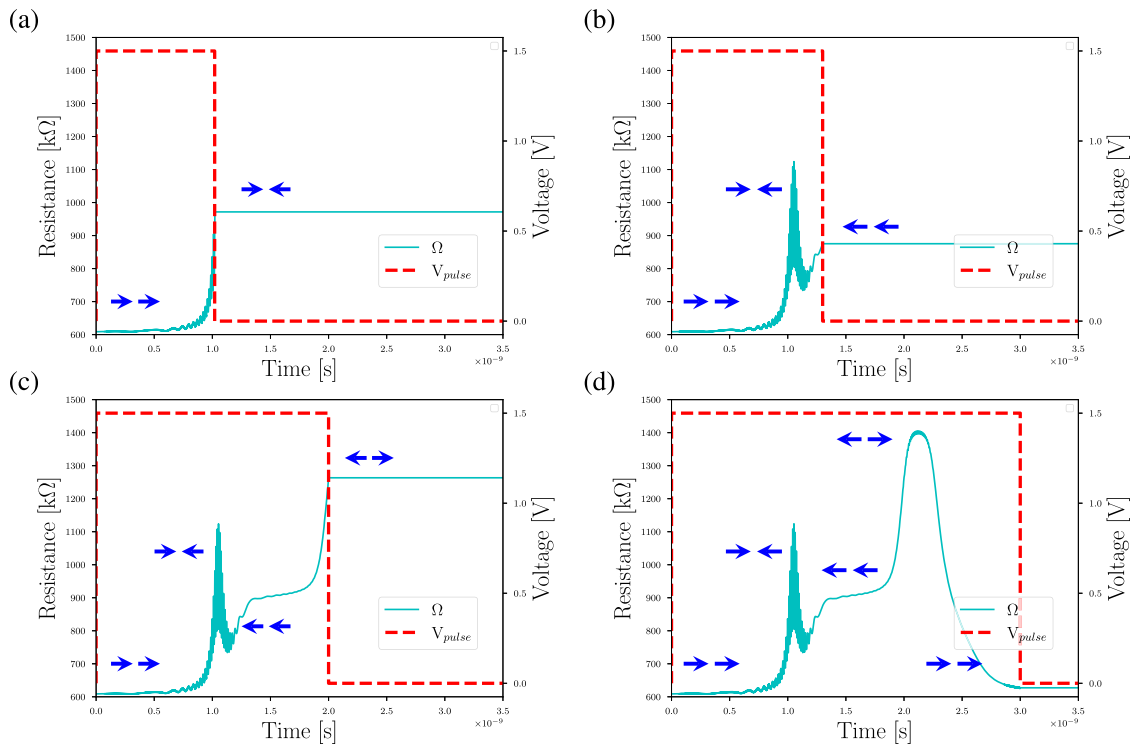
Fig. 6. Resistance trajectories with a symmetric structure of 3 nm long FLs, switching from P to AP for different duration of the applied bias. The solid blue line represents the resistance of the cell during the switching process and the red dashed line the duration and amplitude of the bias pulse. The arrows along the trajectories represent the state of FL_1 and FL_2.

as signified by the solid line in Fig. 5(b), aim to push FL_1 in AP alignment to RL and FL_2 in P alignment to RL.

The damping-like and field-like components, as signified by the dotted line in Fig. 5(b), represent the elevated polarization in the central TB of Fig. 3(b). Due to the elevated polarization in the middle TB, the behavior of the damping-like and field-like components changes and increases. Here, the damping-like and field-like components in FL_2 aim to align the magnetization in P with the RL, while the damping-like and field-like components in FL_1 push the magnetization in the parallel alignment with the RL. This results in a flip of FL_1, causing the entire FL assembly to return to its original state. This loop repeats for the duration of the applied bias.

Therefore, with heightened TB polarization, a stronger spin current emerges, exerting a larger torque at the FL_1 and FL_2 interface, compared to the RL and FL_1 interface. Consequently, when the middle TB's polarization peaks, the back-hopping phenomenon in the FL segments manifests more easily.

In Fig. 6 we report switching realizations with different duration of the applied bias pulse. By adjusting the duration of the bias pulse, we can realize a multi-level cell with four distinctly different states. These states of the FL are illustrated by the blue arrows and they follow the same switching procedure as mentioned earlier. By properly modulating the duration of the pulse, all four states can be addressed. A distinction between the two intermediate states can be recognized by the fact that the first state with FL_1 parallel to the RL and anti-parallel to FL_2 has a lower resistance than the state with FL_1 anti-parallel to the RL and FL_2.

4. Conclusion

Employing the coupled spin and charge drift–diffusion approach, supplemented with appropriate boundary conditions for the spin current $\mathbf{J_S}$ at the TB interfaces, we have accurately accounted for the torque's dependence on the relative magnetization orientation inherent to MTJs. This boundary condition is pivotal, enabling us to precisely describe the spin current and spin accumulations in the RL and FLs. It provides a comprehensive framework to capture the intricacies of spin and charge transport while simultaneously considering magnetization dynamics in diverse MTJ stack configurations.

Our studies shed light on the emergence of the back-hopping effect, particularly pronounced in ultra-scaled STT-MRAM devices featuring a composite-free layer. A meticulous analysis of this phenomenon revealed its potential significance in device engineering. Harnessing the back-hopping effect could be transformative, paving the way for developing multi-bit cells capable of adopting four distinct states, thus expanding data storage capabilities and offering new avenues for device functionality. As we venture further into miniaturized spintronics, these insights may prove instrumental in guiding next-generation device design and optimization.

CRediT authorship contribution statement

M. Bendra: Conceptualization, Data curation, Formal analysis, Investigation, Methodology, Software, Visualization, Writing – original draft, Writing – review & editing. **R.L. de Orio:** Software, Writing – review & editing. **S. Selberherr:** Funding acquisition, Resources, Supervision, Writing – review & editing. **W. Goes:** Resources, Software, Supervision, Writing – review & editing. **V. Sverdlov:** Conceptualization, Funding acquisition, Project administration, Resources, Supervision, Writing – review & editing.

Declaration of competing interest

The authors declare that they have no known competing financial interests or personal relationships that could have appeared to influence the work reported in this paper.

Acknowledgments

References

[1] Jung S, Lee H, Myung S, Kim H, Yoon SK, et al. A crossbar array of magnetoresistive memory devices for in-memory computing. Nature 2022;601:211–6. http://dx.doi.org/10.1038/s41586-021-04196-6.

[2] Naik VB, Yamane K, Lee T, Kwon J, Chao R, et al. JEDEC-qualified highly reliable 22nm FD-SOI embedded MRAM for low-power industrial-grade, and extended performance towards automotive-grade-1 applications. In: IEEE international electron devices meeting. 2020, p. 11.3.1–4. http://dx.doi.org/10.1109/IEDM13553.2020.9371935.

[3] Ikegawa S, Nagel K, Mancoff FB, Alam SM, Arora M, et al. High-Speed (400MB/s) and Low-BER STT-MRAM Technology for Industrial Applications. In: IEEE international electron devices meeting. 2022, p. 10.4.1–4. http://dx.doi.org/10.1109/IEDM45625.2022.10019513.

[4] Hu G, Safranski C, Sun JZ, Hashemi P, Brown SL, et al. Double Spin-Torque Magnetic Tunnel Junction Devices for Last-Level Cache Applications. In: IEEE international electron devices meeting. 2022, p. 10.2.1–4. http://dx.doi.org/10.1109/IEDM45625.2022.10019402.

[5] Seo SM, Aikawa H, Kim SG, Nagase T, Ito Y, et al. First Demonstration of Full Integration and Characterization of $4F^2$ 1S1M Cells with 45 nm of Pitch and 20 nm of MTJ Size. In: IEEE international electron devices meeting. 2022, p. 10.1.1–4. http://dx.doi.org/10.1109/IEDM45625.2022.10019549.

[6] Sato H, Yamanouchi M, Ikeda S, Fukami S, Matsukura F, et al. MgO/CoFeB/Ta/CoFeB/MgO recording structure in magnetic tunnel junctions with perpendicular easy axis. In: IEEE transactions on magnetics, vol. 49, 2013, p. 4437–40. http://dx.doi.org/10.1109/TMAG.2013.2251326.

[7] Jinnai B, Igarashi J, Watanabe K, Funatsu T, Sato H, et al. High-performance shape-anisotropy magnetic tunnel junctions down to 2.3 nm. In: IEEE international electron devices meeting. 2020, p. 24.6.1–4. http://dx.doi.org/10.1109/IEDM13553.2020.9371972.

[8] Abert C, Sepehri-Amin H, Bruckner F, Vogler C, Hayashi M, et al. Back-hopping in spin-transfer-torque devices: Possible origin and countermeasures. Phys Rev Appl 2018;9:054010. http://dx.doi.org/10.1103/PhysRevApplied.9.054010.

[9] Chiu Y-C, Yang C-S, Teng S-H, Huang H-Y, Chang F-C, et al. A 22nm 4Mb STT-MRAM data-encrypted near-memory computation macro with a 192GB/s read-and-decryption bandwidth and 25.1-55.1TOPS/W 8b MAC for AI operations. In: IEEE international solid-state circuits conference, vol. 65, 2022, p. 178–80. http://dx.doi.org/10.1109/ISSCC42614.2022.9731621.

[10] Cai W, Wang M, Cao K, Yang H, Peng S, et al. Stateful Implication Logic Based on Perpendicular Magnetic Tunnel Junctions. In: Sci. China inf. sci., vol. 65, 2022, 122406. http://dx.doi.org/10.1007/s11432-020-3189-x.

[11] Kolev T, Dobrev V. MFEM: Modular finite element methods library. 2024, http://mfem.org. [Accessed: 24 March 2024].

[12] ViennaSpinMag. An open access finite element-based application for calculating the magnetization dynamics of multi-layered structures composed of ferromagnets, metal spacers and tunnel barriers. 2024, https://www.iue.tuwien.ac.at/viennaspinmag/. [Accessed: 24 March 2024].

[13] Ender J, Mohamedou M, Fiorentini S, de Orio RL, Selberherr S, et al. Efficient Demagnetizing Field Calculation for Disconnected Complex Geometries in STT-MRAM Cells. In: International conference on simulation of semiconductor processes and devices. 2020, p. 213–6. http://dx.doi.org/10.23919/SISPAD49475.2020.9241662.

[14] ViennaDemag. An open access demagnetization field solver. 2024, https://www.iue.tuwien.ac.at/viennademag/. [Accessed: 24 March 2024].

[15] Fiorentini S, Bendra M, Ender J, de Orio RL, Goes W, et al. Spin and charge drift-diffusion in ultra-scaled MRAM cells. Sci Rep 2022;12:20958. http://dx.doi.org/10.1038/s41598-022-25586-4.

[16] ViennaSCDD. An open access spin-charge drift-diffusion solver. 2024, https://www.iue.tuwien.ac.at/viennascdd/. [Accessed: 24 March 2024].

[17] Bendra M, Fiorentini S, Selberherr S, Goes W, Sverdlov V. A multi-level cell for ultra-scaled STT-MRAM realized by back-hopping. 208, 2023, 108738. http://dx.doi.org/10.1016/j.sse.2023.108738,

[18] Lepadatu S. Boris computational spintronics online materials database. 2024, http://www.boris-spintronics.uk/online-materials-database/. [Accessed: 24 March 2024].